2021-07

Limitations of small-scale yielding for fatigue crack growth

Marques, B

Limitations of SSY for fatigue crack growth

B Marques[1], MF Borges[1], FV Antunes[1*], JM Vasco-Olmo[2], FA Díaz[2], MN James[3, 4]

[1] University of Coimbra, Centre for Mechanical Engineering, Materials and Processes (CEMMPRE), Department of Mechanical Engineering.

[2] Departamento de Ingeniería Mecánica y Minera, University of Jaén, Jaén, Spain.

[3] School of Engineering, University of Plymouth, Plymouth, United Kingdom.

[4] eNtsa, Nelson Mandela University, Port Elizabeth, South Africa.

*corresponding author: fernando.ventura@dem.uc.pt

Abstract

The work described here has led to a simple criterion that defines the boundary of the small-scale yielding, SSY, regime to avoid invalid use of the LEFM parameter, ΔK, as the characterising parameter for fatigue crack growth rate. The approach proposed is based on the analysis of crack tip opening displacement, CTOD, and its separation into elastic and plastic components. SSY conditions are shown to dominate when the elastic component of CTOD is larger than 75% of the total CTOD measured at a distance of 8 μm (the finite element mesh size) behind the crack tip, i.e., $\Delta\delta_e/\Delta\delta_t$ >75%. Large-scale yielding, LSY, conditions become dominant for relatively large values of plastic CTOD, $\Delta\delta_e/\Delta\delta_t$ <60%. An increase in crack length (and therefore of ΔK), a decrease in yield stress of the material and the existence of plane stress conditions all promote LSY. The results obtained from various loading and geometric conditions simulated in this work demonstrate that caution should be used in assuming that the use of ΔK is valid even for high strength alloys like Ti6Al4V. In this material, the boundary of the elastic regime was crossed and SSY conditions lost, for the longest crack lengths studied and in the case of overloads.

Keywords: Small-scale yielding; Large-scale yielding; Linear elastic fracture mechanics; Stress intensity factor; Crack tip opening displacement

NOMENCLATURE

a = crack length

a_0 = initial crack length

CT = Compact Tension (specimen)

CTOD = Crack Tip Opening Displacement

d = distance to crack tip measured along crack flank

E = Young's modulus

FCGR = Fatigue Crack Growth Rate

K = stress intensity factor

K_C = fracture toughness

K_{max} = maximum stress intensity factor

K_{min} = minimum stress intensity factor

LEFM = Linear Elastic Fracture Mechanics

R = Stress ratio

LSY = Large-Scale yielding

SSY = Small-Scale yielding

t = specimen's thickness

W = specimen's width

Y_0 = Initial yield stress

$\Delta\delta_e$ = elastic range of CTOD

$\Delta\delta_p$ = plastic range of CTOD

$\Delta\delta_t$ = total range of CTOD

ν = Poisson's ratio

ΔK = stress intensity factor range (K_{max}-K_{min})

ΔK_{th} = fatigue threshold

1. Introduction

The application of linear elastic fracture mechanics (LEFM) rests on an assumption that the overall specimen response is linear elastic, even if this does not hold true for a limited region at the crack tip. In LEFM, the stress intensity factor, K, quantifies the magnitude of the $r^{-\frac{1}{2}}$ singularity present in the elastic stress and strain fields [1]. This parameter K has found extensive utility in assessing the potential for fracture, because it includes the effect of crack length and load level, is relatively easy to determine numerically or experimentally, and published solutions are readily available for many different geometries [2-4]. In the study of fatigue crack growth rate (FCGR), the range of stress intensity factor, ΔK, is widely assumed to represent the crack driving force.

The simplicity of its use, based on International Standards [e.g. 5, 6], also explains the long-held dominance of ΔK in FCGR studies. Since Paris and Erdogan proposed their original model [7], a very large number of analytical and empirically-derived models have been proposed that link FCGR with various loading parameters. Fracture toughness, K_C, and fatigue threshold, ΔK_{th}, have been included in the models to provide an improved fit to the sigmoidal shape of the growth rate curve [e.g. 8-11]. The effect of stress ratio was incorporated into the models via the concept of crack closure [12].

Other authors have proposed a two parameter driving force, particularly for fatigue crack growth in less ductile alloys where the maximum stress intensity factor, K_{max}, is likely to have a role in the influence of stress ratio in addition to the range of stress intensity, ΔK [13,14]. Christopher *et al.* [15] proposed a novel mathematical model of the stresses around the tip of a fatigue crack (CJP model), which was intended to address, more completely, the physical mechanisms involved in fatigue crack growth in ductile materials, and hence considers the effects of wake contact and compatibility-induced stresses at the elastic–plastic boundary on the surrounding elastic field. Several

3

parameters were defined from the applied forces to characterize the effective stress field: an opening mode stress intensity factor K_F that drives crack growth, a retarding stress intensity factor, K_R and the T-stress. In essence, whilst the complexity of the various models has been steadily increasing to incorporate identified effects of the plastic region induced at the crack tip during fatigue crack growth, they generally retain the concept of dominance by a stress intensity parameter in the near tip region and assume that LEFM applies, i.e. that the concept of similitude will hold true.

The fundamental difficulty in FCGR studies arises from the hysteretic energy loss associated with crack growth under cyclic loading. In ductile alloys, this is evidenced in irrecoverable plastic deformation at the crack tip. As illustrated schematically in Figure 1, different regions can be identified ahead of a fatigue crack tip [16]. In regions I and II the response of the body is elastic and this region can be divided into two zones, with region I representing the far-field elastic case and region II representing the near-tip K-dominated elastic field. Region III contains the monotonic plastic zone that occurs during the tensile half-cycle of loading. The cyclic plastic zone that occurs under reversed loading is represented by region IV, and this is where there is hysteretic energy loss and crack growth initiates.

Small-scale yielding (SSY) conditions are considered to dominate when the plastic region is small compared to significant dimensions of the body. The plastic zone can be considered as causing a small perturbation in the linear elastic field [17], and Rice [18] showed that under SSY conditions cyclic plasticity at the crack tip is, indeed, controlled by the value of $\varDelta K$. This means that LEFM is valid, i.e. that linear elastic behaviour can be assumed to hold true up to a distance of perhaps twice the plastic zone size from the crack tip. On the other hand, if the plastic deformation is large and extends over region II, LEFM is no longer valid and alternative parameters are needed to quantify the crack

driving force. In other words, with the increase of crack tip plastic zone, SSY no longer holds and the situation moves to Large-Scale Yielding (LSY) conditions.

Under LSY, alternative crack driving parameters are needed, like ΔJ [19], CTOD [20], the energy dissipated [21], net-section cyclic strain energy [22] or even the size of crack tip plastic zone [23]. LSY is more likely to occur in ductile alloys, while in higher strength materials, SSY may be expected. Additionally, an efficient utilization of the materials implies high overall stresses, which favours LSY.
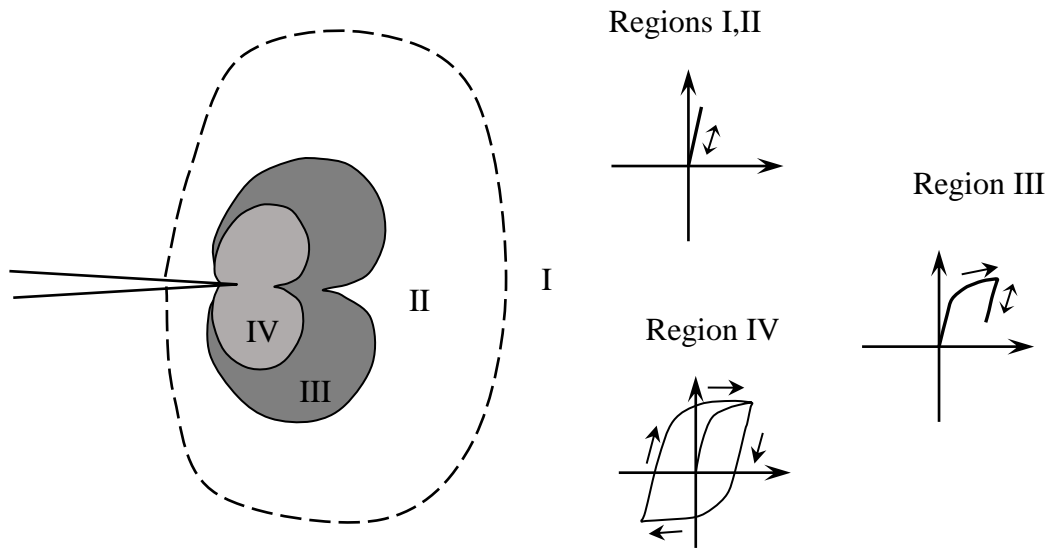

Figure 1. Schematic diagram of crack tip zones, parameters and stress-strain response.

However, the definition of the limits of applicability of LEFM/SSY regime is not straightforward. In fact, the ASTM E647-15 standard [5] indicates that the "conditions giving rise to the each of these two regions (SSY and LSY) of behaviour are not clearly defined". In most published works, the validity of SSY assumption is not checked. It is equally true that when LSY approaches are used the LSY condition limit is not checked [24-26] and, eventually, SSY approaches may have to be used in such studies. Objective criteria are therefore needed to define the boundaries of the LSY and SSY regimes.

According to Dowling [27], in SSY the plastic zone must be "small" compared to the distance to the specimen boundaries. A distance of $4r_p$ is proposed to be a sufficient minimum, where r_p is the size of crack tip plastic zone. Therefore, following Irwin and assuming that for plane stress conditions:

$$r_p = \frac{1}{\pi}(\frac{K}{Y_0})^2 \qquad (1)$$

the minimum required dimensions of the specimen and crack are:

$$a, (W-a), h \geq \frac{1}{4\pi}(\frac{K}{Y_0})^2 \qquad (2)$$

Ritchie [17] proposed that the plastic zone should be ≈ 15 times smaller than the in-plane dimensions of crack length, a, and uncracked ligament $(W-a)$. Note that many solutions have been proposed in published literature for the size of crack tip plastic zone that gives a SSY state. Empirically, it has been proposed that LEFM is valid if:

$$r_p < \frac{a}{50} \text{ to } \frac{a}{30} \qquad (3)$$

The ASTM E647–15 standard [5] states that for results of a K calculation to be valid, the dimensions of C(T) and M(T) specimens should meet the following criteria, respectively:

$$(W-a) \geq \frac{4}{\pi}(\frac{K_{max}}{Y_0})^2 \qquad (4)$$

$$(W-2a) \geq 1.25\frac{F_{max}}{tY_0} \qquad (5)$$

where K_{max} is the maximum stress intensity factor, F_{max} is the maximum force, W is the width of specimen, t is the thickness of specimen, a is the crack length and Y_0 the yield stress of the material. Note that an older version of ASTM stated different criteria, which were:

$$a, h, (W-a) \geq \frac{4}{\pi}(\frac{K_{max}}{Y_0})^2 \qquad (6)$$

$$a, h, (W - 2a) \geq 1.25 \frac{F_{max}}{tY_0} \tag{7}$$

Therefore, not only the remaining ligament, but all the distances to free surfaces were limited, as Figure 2 illustrates. If these criteria are not met, then LEFM cannot be applied.
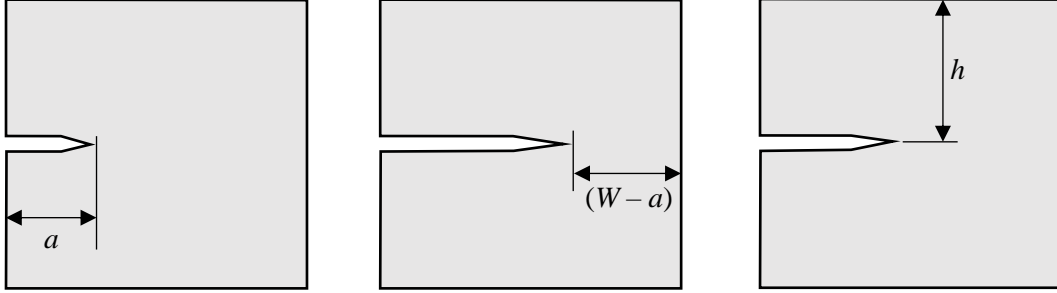

Figure 2. Situations where the LEFM is not valid, according ASTM E647 (CT and MT specimens).

The main objective in the current work is the definition of the boundaries of the SSY and LSY regimes to avoid an invalid use of the stress intensity factor range as a parameter to characterise fatigue crack propagation. A closed form solution is not easy to obtain, because the material properties, the loading parameters and the geometry all influence crack tip plastic deformation. Therefore, instead of a closed form solution a procedure is proposed to check the boundaries of the SSY and LSY regimes using the crack tip opening displacement (CTOD). The CTOD, obtained numerically using the finite element method or experimentally using DIC, is separated into its elastic and plastic components. Note that the classical approach based on the size of crack tip plastic zone is replaced here by the crack tip plastic deformation, quantified by the plastic component of CTOD. However, a strong link is expected between the plastic CTOD and the size of crack tip plastic zone [28], so both approaches are viable. In order for the LEFM to be applicable, it is necessary that the plastic CTOD range is relatively small.

2. Criteria to define the boundary between the SSY and LSY regimes

2.1. Numerical modelling

A standard compact C(T) specimen geometry was used in the work to define a criterion to predict the SSY/LSY boundary, as illustrated in Figure 3a. The specimen is symmetrical in both the vertical and horizontal planes and therefore only 1/4 of the specimen has to be simulated using appropriate boundary conditions. A small specimen thickness was used ($t = 0.1$ mm) to give a plane stress state. A plane strain situation was also modelled by constraining out-of-plane deformation on both faces of the specimen and crack closure was allowed to occur in the modelling. Three specimen configurations (*A*, *B* and *C*) were considered, as indicated in Table 1. Configurations *B* and *C* have the same specimen width, *W*, but different initial crack lengths, a_0. The loading conditions and materials are indicated in Table 2. The total number of the cases considered was 171.
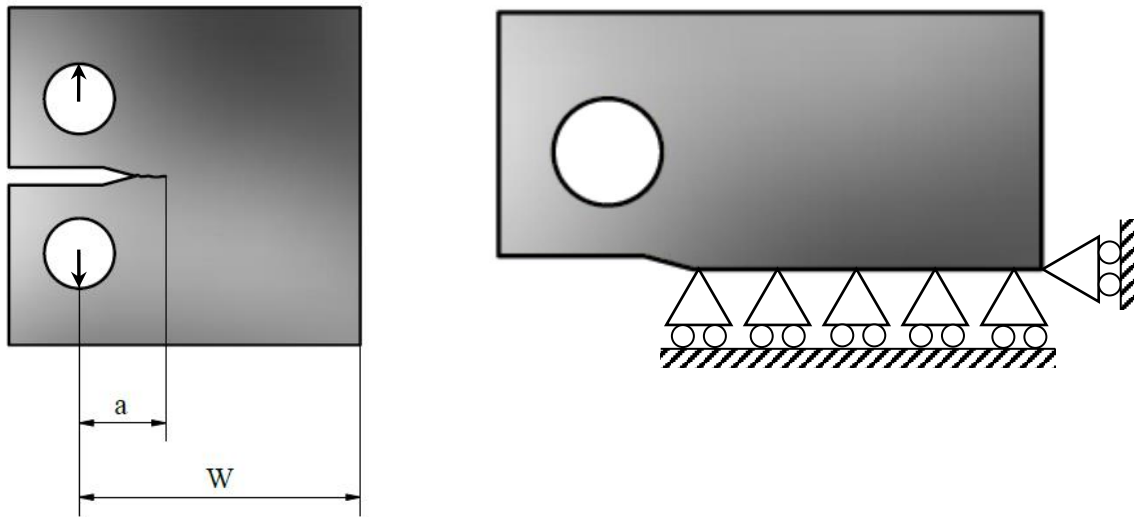

Figure 3. CT specimen (a) Main dimensions. (b) Boundary conditions.

Table 1. Specimens configuration.

Specimen config.	Type	W [mm]	t [mm]	a_0 [mm]
A	C(T)	36	0.1	7, 10, 13, 16, 19, 22, 24
B	C(T)	50	0.1	5, 9, 12.5, 14, 16.5, 19, 21.5, 24, 26.5, 29
C	C(T)	50	0.1	13.25, 15, 16.25, 17.5, 20, 22.5, 25, 30

Table 2. Loading conditions.

Material	Specimen config.	R	ΔK [MPa.m$^{0.5}$]	F_{min} [N]	F_{max} [N]	Stress State
2050-T8	A	0.05	11.3 up to 53.4	2.48	49.61	Plane stress
2024-T351	B	0.1 up to 0.7	4.2 up to 21.7	4.17 up to 72.92	41.67 up to 104.17	Plane strain, Plane stress
304L SS	C, A	0.1 up to 0.7	5.8 up to 53.0	-11.15 up to 166.10	11.81 up to 237.29	Plane strain, Plane stress
7050-T6	A	0.05	11.2 up to 53.4	2.48	49.61	Plane stress
6082-T6	A	0.05	11.2 up to 22.2	2.48	49.61	Plane stress
18Ni300	A	0.05	11.1 up to 51.2	2.48	49.61	Plane strain, Plane stress

Elastic-plastic models were used for the materials shown in Table 2, which have been chosen to represent a broad range of alloys and include work hardening and heat-treatable aluminium alloys, an austenitic stainless steel and a maraging steel. In addition, the criterion obtained was validated against a simulation using Ti6Al4V titanium alloy. In these simulations elastic behaviour followed a generalized Hooke's law and plastic behaviour was governed by the Huber-Mises yield criterion coupled with isotropic and

kinematic hardening, under an associated flow rule. The kinematic behaviour is given by the Armstrong-Frederick hardening law [29]:

$$\dot{X} = C_X \left[X_{Sat} \frac{\sigma\prime - X}{\bar{\sigma}} - X \right] \dot{\bar{\varepsilon}}^p,$$ (8)

where C_X and X_{Sat} are the material parameters of Armstrong-Frederick law, $\sigma\prime$ is the Cauchy stress tensor, X is the back stress tensor, $\bar{\sigma}$ is the equivalent stress and $\dot{\bar{\varepsilon}}^p$ is the equivalent plastic strain rate.

Table 3 gives the isotropic behaviour for the various materials in terms of the Voce hardening law [30], as follows:

$$Y = Y_0 + (Y_{Sat} - Y_0)[1 - exp(-C_Y \bar{\varepsilon}^p)],$$ (9)

where Y_0 is the yield stress, Y_{Sat}, and C_Y are material parameters in the Voce law and $\bar{\varepsilon}^p$ is the equivalent plastic strain. Table 4 gives the equivalent isotropic behaviour of the materials in terms of the Swift hardening law [31], as follows:

$$Y = C \left[\left(\frac{Y_0}{C} \right)^{\frac{1}{n}} + \bar{\varepsilon}^p \right]^n,$$ (10)

where C and n are material parameters in the Swift law. The values of the elastic-plastic properties found in Tables 3 and 4 were obtained by fitting experimentally obtained stress-strain loops from smooth cylindrical specimens.

Table 3. Material properties with isotropic hardening fitted with Voce law.

Material	Hooke's law		Isotropic hardening (Voce)			Kinematic Hardening (Armstrong-Frederick)	
	E [GPa]	v [-]	Y_0 [MPa]	Y_{Sat} [MPa]	C_Y [-]	C_X [-]	X_{Sat} [MPa]
2050-T8 [32]	70.40	0.30	383.9	383.85	0	95.38	265.41
304L SS [33]	196	0.30	117	204	9	300	176
7050-T6 kinematic [34]	69.724	0.30	420.5	420.5	3.806	228.91	198.35
7050-T6 isotropic	69.724	0.30	420.5	420.5	3.806	0	0
6082-T6 [35]	70	0.29	238.15	487.52	0	244.44	83.18
18Ni300 SLM [36]	165	0.30	1000	1000	0	728.34	402.06

Table 4. Material properties with isotropic hardening fitted with Swift law.

Material	Hooke's law		Isotropic hardening (Swift)			Kinematic Hardening (Armstrong-Frederick)	
	E [GPa]	v [-]	Y_0 [MPa]	C [MPa]	n [-]	C_X [-]	X_{Sat} [MPa]
2024-T351	72.261	0.29	288.96	389	0.056	138.8	111.84
Ti6Al4V HIP	115	0.33	823.50	707.07	-0.0288	104.26	402.01
Ti6Al4V heat treatment	115	0.33	700	738.57	-0.013	88.07	585.18

The finite-element mesh was refined near the crack tip and enlarged for more remote positions. Square elements with dimensions of 8×8 μm were used in the refined regions. This element size was chosen as a compromise between increased computation time with a smaller mesh size and a the first node being relatively too far from the crack tip with a larger mesh size. Only one layer of elements was considered through the thickness. Crack propagation was simulated by successive debonding of nodes at the

minimum load. The FCG rates obtained assuming propagation at minimum load were compared with similar results obtained with propagation at maximum load, and showed no effect of this numerical parameter [37]. Each crack increment corresponded to one finite element, and either two or five load cycles were applied between increments. The FCG rate is artificially constant and lower than real values, because the main objectives were the stabilization of crack tip fields and the formation of a residual plastic wake. At the end of each cycle, the crack propagates uniformly through the thickness by releasing both current crack front nodes. The numerical simulations were performed with the three-dimensional elastic–plastic finite-element programme DD3IMP, originally developed to simulate deep drawing. Further details of this numerical procedure may be found in the literature [32-36].

The CTOD was measured at the first node behind crack tip, i.e. at a distance of 8 μm. Figure 4 presents a typical curve of CTOD versus applied load. At minimum load (*A*) the crack is closed, i.e. there is no CTOD at the first node behind crack tip. An increase of load opens the crack at point *B*. After opening, there is a linear displacement region (*B-C*) linked to the elastic behaviour of the material. Microplastic deformation starts after point *C*, increasing monotonically up to the maximum load (*D*). The elastic CTOD is then obtained from extrapolating the elastic behaviour defined between points C and D (illustrated by the solid line) up to the maximum load; the plastic CTOD is obtained by subtracting the elastic CTOD from the total CTOD. The elastic and plastic CTOD ranges, $\Delta\delta_e$ and $\Delta\delta_p$ respectively, are indicated in Figure 4. Marques *et al* [38] made a detailed analysis of the procedure recommended to obtain accurate values of $\Delta\delta_e$ and $\Delta\delta_p$. The total CTOD range, $\Delta\delta_t$, is the sum of elastic and plastic components:

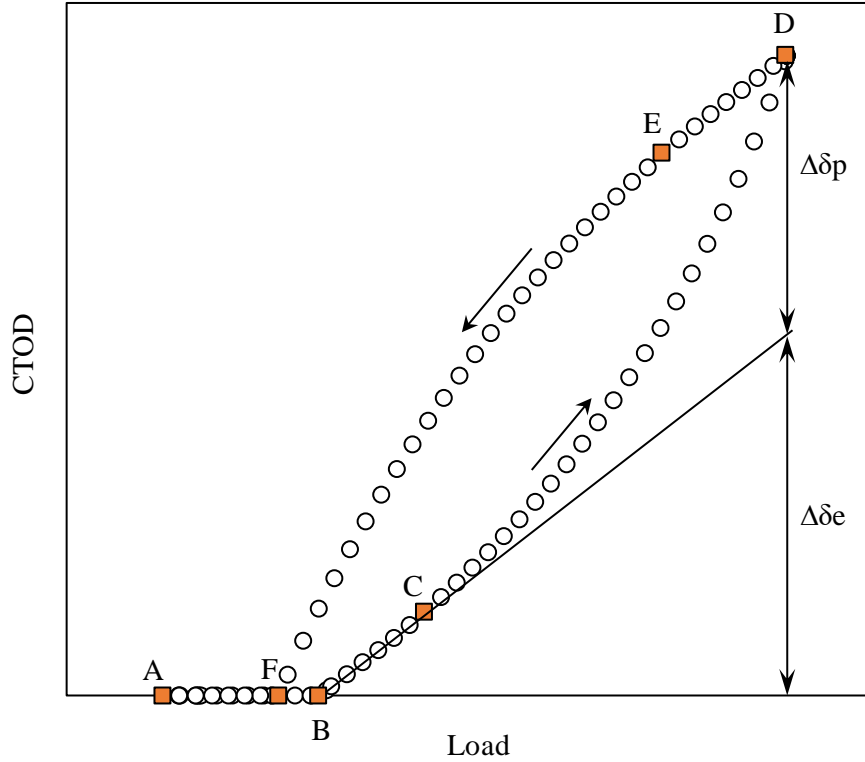$$\Delta\delta_t = \Delta\delta_e + \Delta\delta_e \tag{11}$$

Figure 4. Typical plot of CTOD versus applied load.

The elastic and total CTOD ranges, $\Delta\delta_e$ and $\Delta\delta_t$, respectively, were used to define a new parameter:

$$\%\Delta\delta_e = \frac{\Delta\delta_e}{\Delta\delta_t} \times 100 \tag{12}$$

This parameter has a value of 100% when the CTOD is totally elastic and a value of zero when it is totally plastic. It is, therefore, a useful parameter to study the transition from SSY to LSY. A similar approach to that shown in Figure 4 was followed by Escalero *et al* [39] in determining the boundary between SSY and LSY. They used finite element modelling of a hole-edge crack configuration with firstly linear elastic and secondly elastic-perfectly plastic material behaviour and used the elastic and plastic components of the J-integral to verify the limit of validity of the SSY assumption by plotting J-integral versus crack length. The boundary of SSY was defined by the separation of the curves

for the elastic and plastic components. An arbitrary criterion of a difference between the two curves of 2% was considered as the boundary.

2.2. Validation of the defined criteria

An objective criterion is needed that defines the boundary of SSY. Recalling from Equation 12 that $\%\Delta\delta_e$ indicates the relative level of plasticity at the crack tip (0% being totally plastic), Figure 5 presents a histogram showing the frequency distribution of the number of simulated loading cases for different ranges of $\%\Delta\delta_e$. As can be seen, the values of $\%\Delta\delta_e$ range from 30% to 100%, with the greatest frequency occurring at a range of 70-75%. A second histogram series is included in Figure 5, representing the frequency of cases where LEFM is invalid, in terms of the requirements of ASTM E647–15. This series is termed "LEFM n/a" where "n/a" means not applicable. For values of $\%\Delta\delta_e$ below 60%, virtually all the cases are invalid. For values of $\%\Delta\delta_e$ between 60% and 75-80%, the SSY assumption is invalid for some of the simulated loading cases. Above 80% all the simulated loading cases are valid in LEFM terms.

Considering these data, the following rule can be proposed: for $\%\Delta\delta_e$ values above 75% LEFM is applicable, while for $\%\Delta\delta_e$ values below 60% LEFM is no longer applicable, and the range between 60% and 75% defines a transition regime from LSY to SSY. Manipulating equations 11 and 12 gives:

$$\frac{\delta_p}{\delta_e} = \frac{1}{\%\Delta\delta_e} - 1 \tag{13}$$

Equation 13 shows that the lower boundary proposed for the SSY regime ($\%\Delta\delta_e = 75\%$) is equivalent to $\delta_p/\delta_e = 33\%$.
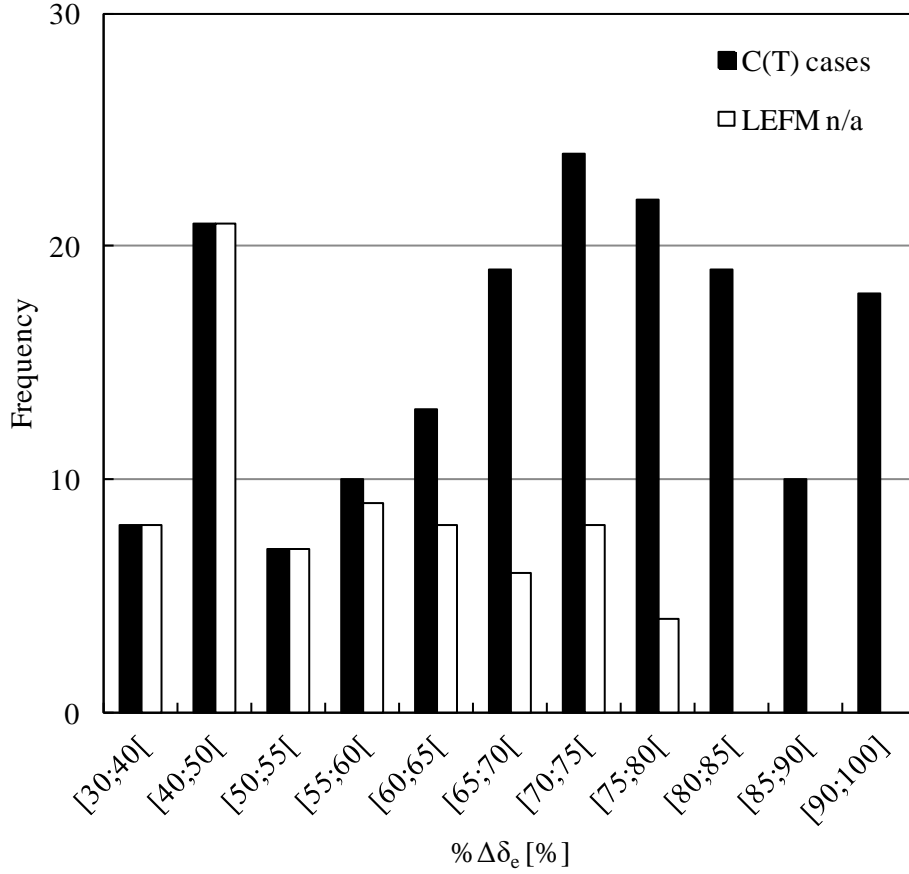
Figure 5. Histogram of the values of *%Δδₑ* and of invalid cases according ASTM E647–15.

Figure 6 presents a graph of $\Delta\delta_t$ versus $\Delta\delta_e$. The solid line has a slope of 45°, representing the situation where $\Delta\delta_t = \Delta\delta_e$, i.e. the CTOD is totally elastic. The dashed lines indicate the boundaries of the SSY and LSY regimes, defined using the rule proposed in this paper. The region between the 45° line and the line with longer dashes is the SSY regime (i.e. $\%\Delta\delta_e > 75\%$). The increase in the stress intensity range ΔK produces a progressive increase of plastic deformation, as would be expected. There are a significant number of data points which fall into the invalid region of $\%\Delta\delta_e$ and they cannot be defined simply in terms of the value of applied stress intensity range.
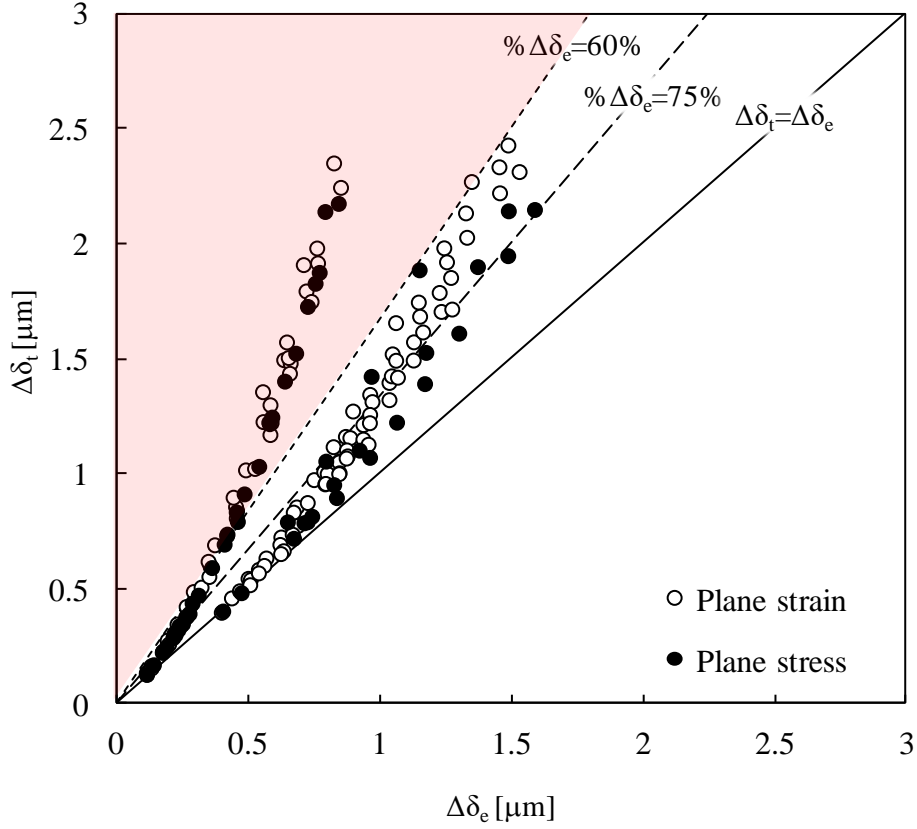
Figure 6. Representation of $\Delta\delta_t$ as a function of $\Delta\delta_e$.

The effect of crack length on $\%\Delta\delta_e$ is illustrated in Figure 7, which presents results for the 2050-T8 aluminium alloy. As in Figure 6, the line with longer dashes represents the boundary proposed for the SSY regime. An increase in crack length at a given value of applied stress range progressively increases ΔK, and the data indicate a transition from SSY conditions at a crack length of approximately 21 mm. For the two longest crack lengths, the use of LEFM and ΔK is questionable. Note that the increase in crack length produces a progressive change from a state of plane strain state to one of plane stress, where the biaxial stress state makes plastic deformation easier compared with the triaxial stress state in plane strain.
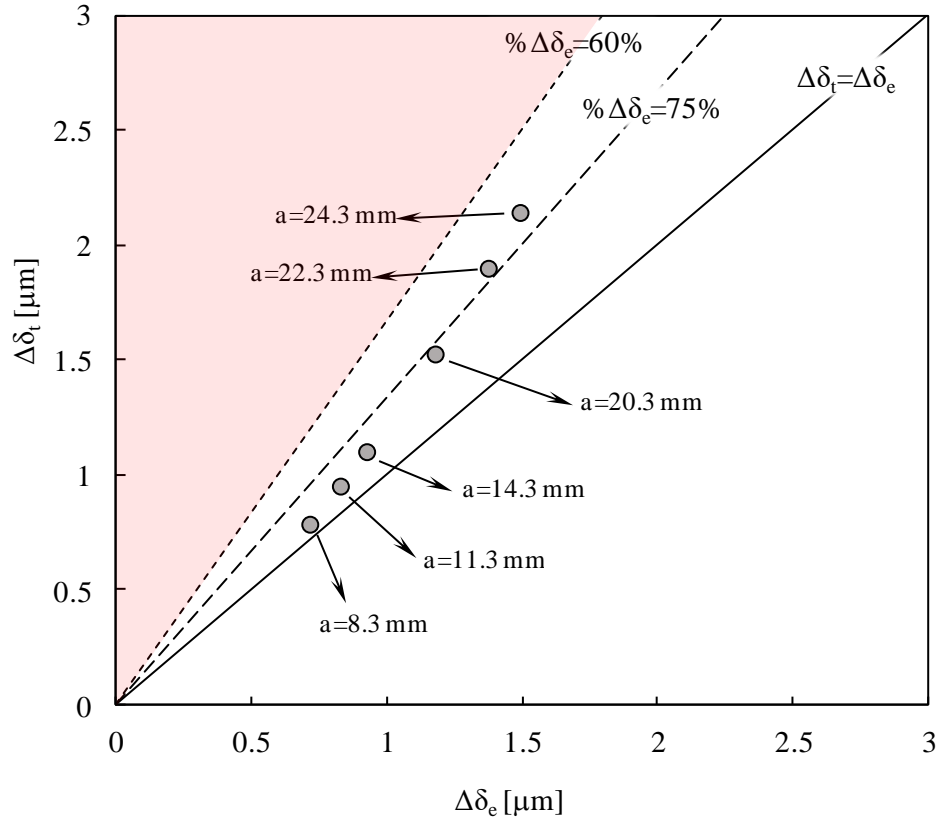
Figure 7. Effect of crack length on the relation between the elastic and total ΔK (2050-T8; CT36; plane stress; R=0.05).

Figure 8 shows the effect of stress state and it is clear that a triaxial plane strain stress state leads to less plastic deformation at a given value of $\Delta\delta_t$ than a state of biaxial plane stress. Therefore, for the same geometry, material and loading conditions, ΔK has less problems of validity than for plane stress state.
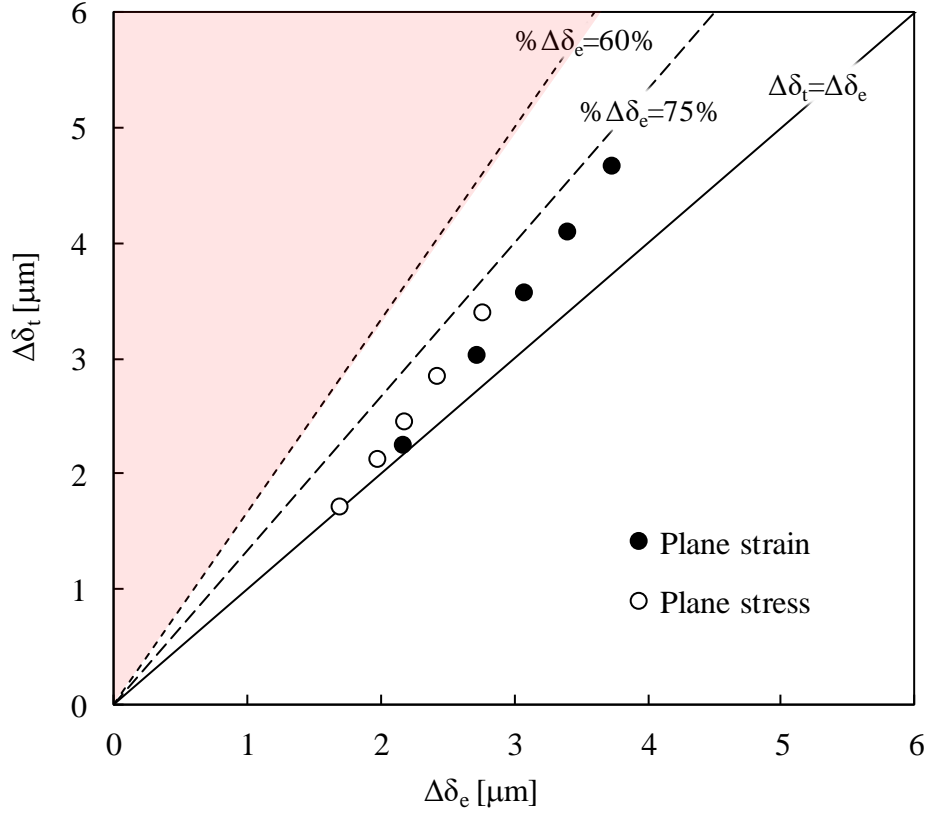
Figure 8. Effect of stress state on the relation between the elastic and total CTOD
(AA2050-T8; MT160; *R*=0.1; a_0= 5, 10, 15, 20, 25 mm).

Figure 9 illustrates the effect of yield stress and presents data from the three alloys
simulated in this work with the same CT geometry, crack lengths and loading. The three
materials have different mechanical properties, with the yield stress being the most
relevant in work that considers the SSY boundary. The values of initial yield stress, Y_0,
for the 304L stainless steel (SS), 7050-T6 aluminium alloy (AA) and 18Ni300 steel are
117 MPa, 420.5 MPa and 1000 MPa, respectively (see Table 3). As expected, an increase
in Y_0 reduces plastic deformation at the crack tip and, for the geometrical and loading
conditions simulated in this work, SSY with *ΔK* as the characterising parameter for
fatigue crack growth rate is clearly applicable in the case of the 18Ni300 steel and the
7050-T6. However, the 304L stainless steel has a relatively low yield stress and the

conditions simulated in the present work lead to values of $\Delta\delta_e$ that lie well outside the SSY regime.
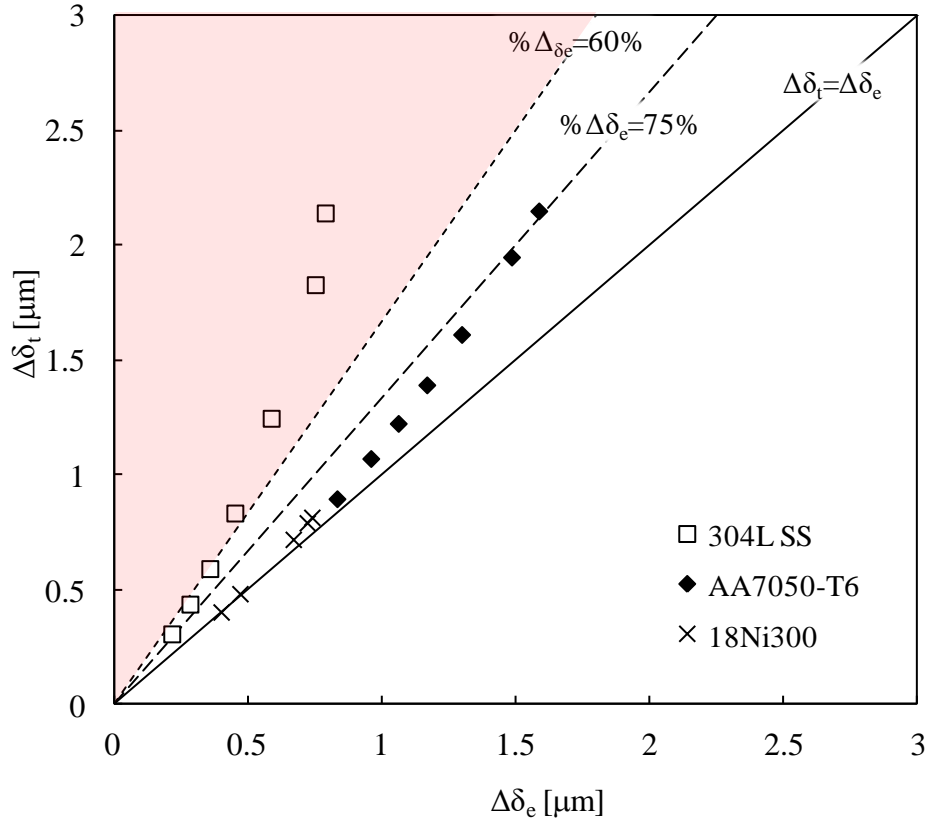

Figure 9. Effect of material's yield stress on the validity of ΔK
(CT36; plane stress; R=0.05; a_0= 7, 10, 13, 16, 19, 22 e 24 mm).

3. Application to the Ti6Al4V titanium alloy

3.1. Numerical model

The methodology outlined above to check the validity of the SSY assumption was also applied to simulation of Ti6Al4V titanium alloy. C(T) specimens with W=36 mm were used with different values of a_0 (Table 1) and with the same boundary conditions illustrated in Figure 3. The simulation considered two alternative post-processing treatments: Hot Isostatic Pressing (HIP) and a heat treatment intended to reduce the residual stresses. These are post-processing treatments that are considered to improve the performance of specimens produced by additive manufacturing techniques [40]. The

19

elastoplastic properties are given in Table 4. Fatigue crack growth was simulated under constant amplitude loading and with single overloads in both plane strain and plane stress states. The constant amplitude loading conditions are given in Table 5. Crack propagation was taken as occurring when the accumulated plastic strain, $\Delta\varepsilon^p$, measured in the vicinity of the crack tip, reached its critical value, $\Delta\varepsilon^p_c$ [37]. The values of $\Delta\varepsilon^p_c$, given in Table 5 were obtained by fitting the experimental values of FCGR, for $a_0 = 22$ mm. This criterion gives realist FCG rates, thereby improving the global quality of the numerical predictions.

Table 5. Constant amplitude loading conditions for the Ti_6Al_4V alloy.

Material	R	F_{min} (N)	F_{max} (N)	ΔK (MPa√m)	$\Delta\varepsilon^p_c$ (%)	Stress State
Ti6Al4V HIP	0.05	2.20	44.05	9.3 – 43.0	85.9	Plane strain
Ti6Al4V HIP	0.05	2.20	44.05	9.3 – 40.9	95.8	Plane stress
Ti6Al4V heat treatment	0.05	2.20	44.05	9.8 – 43.4	40.6	Plane strain
Ti6Al4V heat treatment	0.05	2.20	44.05	9.9 – 41.7	26.6	Plane stress

Overload simulations used the specimen parameters representing a HIP treatment, in plane stress conditions. Overload ratios of 1.5 and 2.0 were considered, where overload ratio is given by:

$$OLR = \frac{\Delta K_{OL}}{\Delta K_{BL}} \tag{13}$$

where ΔK_{OL} and ΔK_{BL} are the overload and constant amplitude stress intensity factor ranges, respectively. The loading conditions relevant to these simulations are given in Table 6 and in these tests, $\Delta\varepsilon^p_c$ was determined by fitting of the experimental FCGR data, for $a_0 = 7$ mm.

Table 6. Loading conditions for the Ti6Al4V alloy, under overloading.

Material	R	F_{min} (N)	F_{max} (N)	F_{OL} (N)	ΔK_{BL} (MPa$\sqrt{m}$)	OLR	$\Delta\varepsilon^p_c$ (%)	Stress State
Ti6Al4V HIP	0.05	2.20	44.05	66.075	18.246	1.5	153.3	Plane stress
Ti6Al4V HIP	0.05	2.20	44.05	88.1	18.274	2	153.3	Plane stress

3.2. Numerical results

3.2.1 Fatigue crack growth under constant amplitude

Figures 10a (HIP simulation) and 10b (residual stress reducing heat treatment) show the results of the Ti6Al4V simulations in terms of the effect of crack length in the transition from SSY to LSY. The increase of crack length is reflected in the increase in the value of ΔK. In both figures, an increase in crack length gives a higher $\Delta\delta_p$ due to the increase in plastic zone size, thereby reducing $\Delta\delta_e/\Delta\delta_t$. For a_0 approximately > 22 mm, SSY is no longer valid.
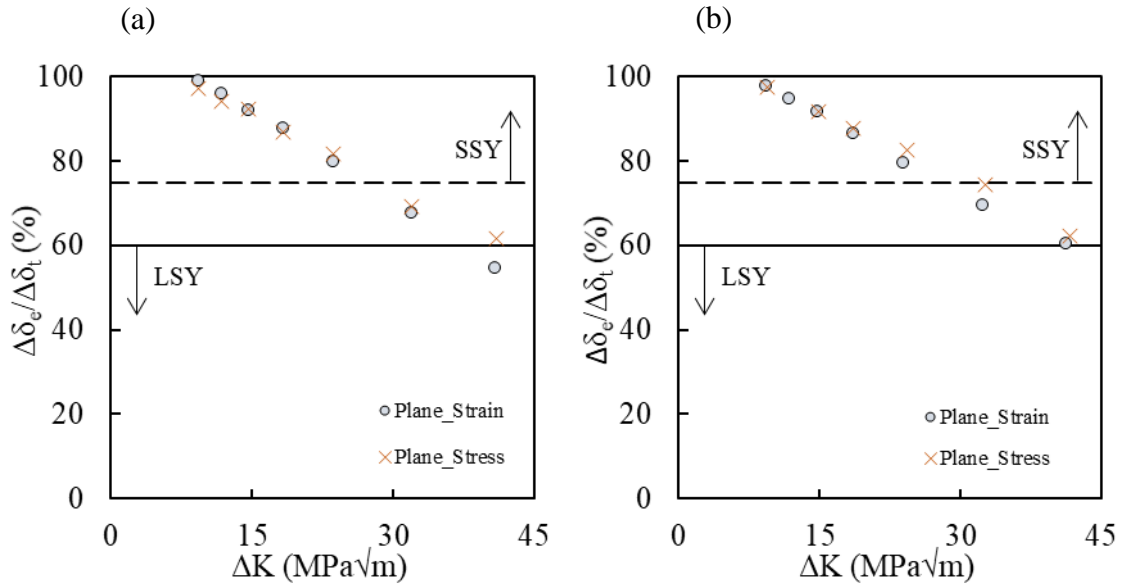

Figure 10. The effect of crack length and stress state on the transition from SSY to LSY for Ti6Al4V: CT36; R=0.05; a_0=7, 10, 13, 16, 19, 22 and 24 mm). (a) HIP manufacturing process; (b) Heat treatment to reduce the residual stresses.

3.2.2 Fatigue crack growth with overload

21

Figure 11a shows the result of an overload in terms of its effect on $\Delta\delta_e/\Delta\delta_t$, and on the numerically predicted values of da/dN and crack closure, as a function of crack length, a. As seen in the graph, initially da/dN decreases with a, corresponding with an increase in U^* and with $\Delta\delta_e/\Delta\delta_t$ remaining in 85%-93% range, i.e. in the SSY regime. U^* represents a closure ratio as a function of the closed portion of the load cycle over the total load range, and is given by:

$$U^* = \frac{F_{open} - F_{min}}{F_{max} - F_{min}} \times 100 \tag{13}$$

where F_{open} is the crack opening load.

At ΔK_{BL}=18.246 MPa√m, an overload of 150% was applied, leading to an instantaneous increase in da/dN and a decrease in U^*, as expected. At the same time, $\Delta\delta_e/\Delta\delta_t$ decreases abruptly to 48%, implying that local crack tip conditions now fall well inside the LSY regime, where ΔK is no longer valid. When the overload is applied, the plastic deformation increases substantially because the material has not previously experienced this loading level. This produces crack tip blunting and a sudden decrease of U^*. Subsequent crack growth through the enlarged plastic zone leads to a transient increase in U^* and therefore a decrease in da/dN, while $\Delta\delta_e/\Delta\delta_t$ rapidly returns to the its pre-overload values. Thereafter, da/dN starts to increase to its original values and the closure ratio U^* decreases. Similar trends were observed with an OLR=2, as shown in Figure 11b, but with increased transients in the graphs. Prior to the overload, both da/dN and $\Delta\delta_e/\Delta\delta_t$ showed similar trends and values to those seen in Figure 11a. The overload was applied at ΔK_{BL}=18.274 MPa√m, resulting in a greater increase in da/dN and corresponding drop in $\Delta\delta_e/\Delta\delta_t$, compared with the data in Figure 11a, as expected.
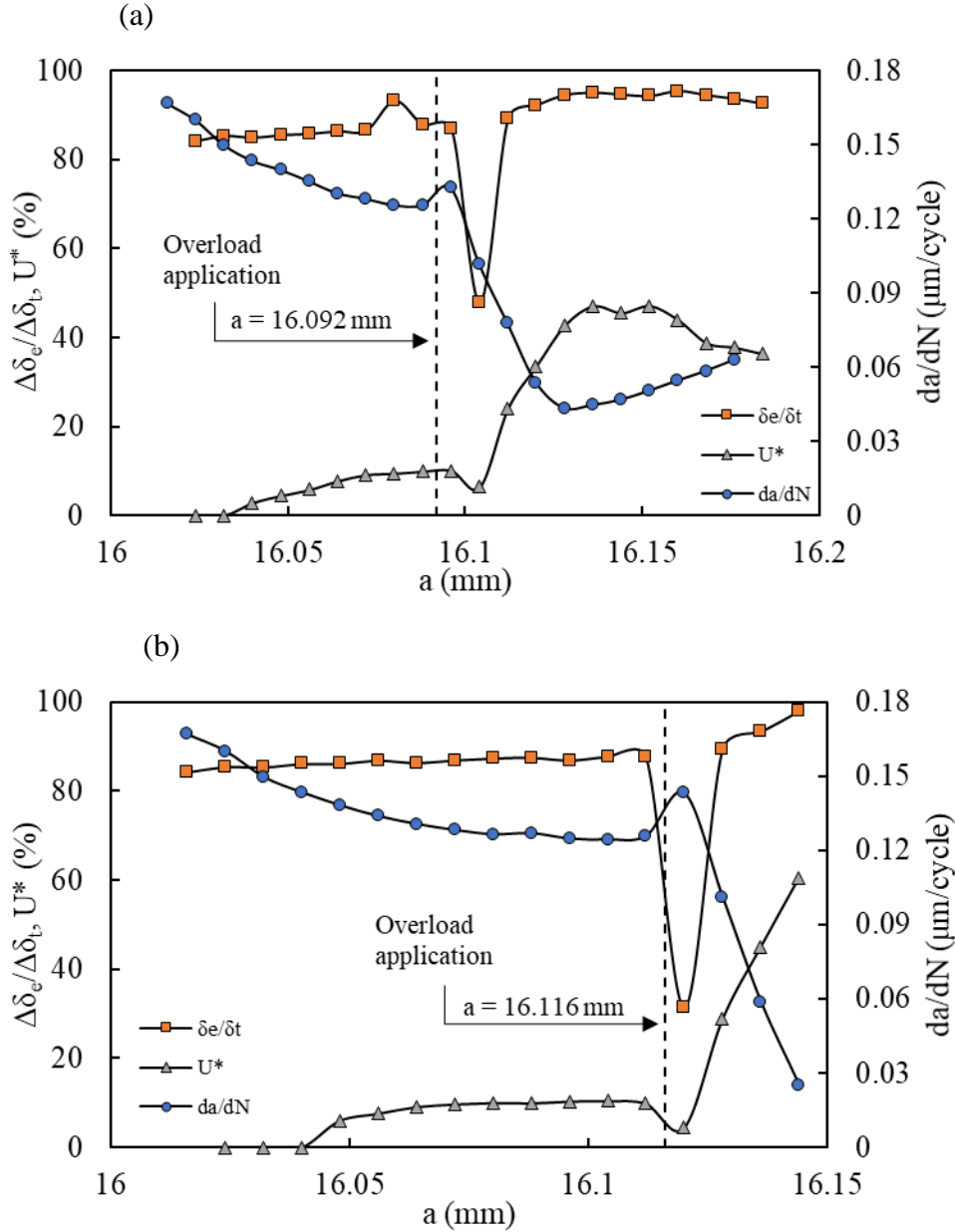
Figure 11. Effect of the application of an overload on $\varDelta\delta_e/\varDelta\delta_t$, da/dN and U^* with $\varDelta a$ (Ti$_6$Al$_4$V; CT36; R=0.05; a_0=16 mm; HIP; plane stress). (a) OLR=1.5; (b) OLR=2.0.

4. Discussion

Traditionally ΔK has been used as a parameter to characterise fatigue crack propagation in applications under SSY conditions with the Paris relationship [7]. SSY conditions require that the extent of nonlinear plastic deformation at the tip of a growing fatigue crack is small enough to establish an overall elastic response of the material. However, in applications where conditions are predominantly plastic (LSY), ΔK is no

longer a valid parameter to describe the conditions at the crack tip and an alternative parameter must be found to correctly characterise fatigue crack growth. Thus, CTOD has been used in this work as parameter to establish whether SSY and LSY conditions can be defined in a crack propagation problem since it has been previously demonstrated [33], both numerically and experimentally, that the plastic component of CTOD can be directly linked with plastic deformation at the crack tip and therefore, $\Delta\delta_p$ is a suitable parameter to characterise fatigue crack growth. Thus, a criterion has been defined in the current work to establish when SSY or LSY conditions can be considered valid. The results obtained have shown that SSY conditions can be defined when the elastic range of CTOD is larger than 75% of the total range of CTOD ($\Delta\delta_e/\Delta\delta_t>75\%$). Additionally, LSY conditions will dominate when $\Delta\delta_e/\Delta\delta_t<60\%$. Between these two defined ranges, it is clear that there is a transition range where both regimes coexist. This transition regime is not surprising since even the ASTM E647-15 standard [5] indicates that SSY or LSY conditions are not clearly defined. The proposed methodology has been validated by studying different materials (2050-T8, 2024-T351, 7050-T6 and 6082-T6 aluminium alloys, and 304L and 18Ni300 steels) subjected to various loading conditions and two stress states. In addition, this methodology has been accurately applied in Ti6Al4V titanium alloy with two different heat treatments and different stress states. For the implementation of the proposed methodology, the ranges of the elastic and plastic components of CTOD are obtained from the analysis of the CTOD plots obtained through a either complete cycle. The CTOD traces can be obtained either numerically by finite element method [35] 0or experimentally by DIC [41].

The approach proposed has been developed and applied to standard specimens, however it is also applicable to more complex geometries. Numerical tools are increasingly evolving and becoming more user-friendly, allowing the study of real

applications. Numerical approaches are also able to include the effects of geometric, loading and material parameters.

5. Conclusions

The objective in this work was to identify an objective criterion that can be used to define the boundary between small-scale yielding (SSY) where linear elastic fracture mechanics (LEFM) can be used and those situations where elastoplastic fracture mechanics (EPFM) is more appropriate. The motivation for the work was the fact that although the range of stress intensity factor (ΔK) is widely used to characterise the driving force for fatigue crack propagation, its validity is rarely checked. An extensive programme of numerical simulation and analysis has been presented, based on CTOD and its separation into elastic and plastic components, that has allowed a clear proposal to be made for a criterion that defines the boundary of SSY and the transition to LSY. This criterion has been successfully applied to compact tension, notched and unnotched SENT specimen geometries in a wide-ranging study that simulated several different aluminium alloys, an austenitic stainless steel and a maraging steel. The criterion found was also checked against a Ti6Al4V titanium alloy. In addition, the work has considered the effects of both constant amplitude loading and spike overloads, and the influence of crack closure.

Detailed conclusions that can be drawn from the work include:

1. A *%$\Delta\delta_e$* parameter was proposed in equation (12) to define the boundary of SSY, and is given by the ratio between $\Delta\delta_e$ and $\Delta\delta_t$. These parameters were obtained from elastic and total CTOD, using Westergaard equations. A value of 100% represents totally elastic behaviour, while a value of zero indicates that the CTOD is totally plastic;

2. Using the elastic and plastic CTOD data from the 171 simulation cases considered in this work, and incorporating the requirements of ASTM E647-15 for valid use of LEFM, a value $\%\Delta\delta_e = 75\%$ is proposed to indicate the lower bound for valid use of the LEFM parameter ΔK;

3. An increase in crack length and/or a decrease in the material's yield stress both promote the onset of LSY;

4. The methodology has been applied to compact tension specimens of Ti6Al4V alloy, showing limitations to the assumption of SSY even for this high strength material. The SSY assumption was also found to be more likely to be invalid when an overload is applied.

Finally, although the conclusions given above are reasonable generalisations, the authors stress that it is important to check the applicability of the SSY assumption for a particular specimen geometry, alloy and loading conditions using the criterion proposed in this paper. The approach proposed to check the validity of SSY assumption can also be implemented using digital image correlation techniques to obtain the CTOD plots.

Acknowledgements

References

[1] Anderson TL. Fracture Mechanics: Fundamentals and Applications. Boca Raton, USA: CRC Press LLC; 2005.

[2] Murakami Y. Stress intensity factors handbook. Oxford [Oxfordshire]; New York: Pergamon Press; 1987

[3] Carpinteri A. Handbook of Fatigue Crack Propagation in Metallic Structures. Elsevier Science, 1994.

[4] Tada H, Paris PC, Irwin GR. American Society of Mechanical Engineers. ASM International. The stress analysis of cracks handbook. 3rd ed. New York: ASME Press: Professional Engineering Pub.: ASM International; 2000.

[5] ASTM E 647-15. Standard test method for measurement of fatigue crack growth rates. Philadelphia: American Society for Testing and Materials (ASTM); 2011.

[6] ISO 12108. Metallic materials – fatigue testing – fatigue crack growth method. Geneva: International Organization for Standardization (ISO); 2012.

[7] Paris PC, Erdogan J. () Critical analysis of crack growth propagation laws. J Basic Eng 1963;85D:528–34.

[8] Erdogan F, Ratwani M. Fatigue and fracture of cylindrical shells containing circumferential crack. Int J Fract Mech. 1970;4:379–392.

[9] Forman R G, Kearney V E, Engles RM. Numerical analysis of crack propagation in cyclic loaded structures. Int J Fract Mech 1967;89:459–464.

[10] Raju KN. An energy balance criterion for crack growth under fatigue loading from considerations of energy of plastic deformation. Int J Fract Mech 1972;8:1–14.

[11] NASGRO, Fracture Mechanics and Fatigue Crack Growth Analysis Software. 2016.

[12] Elber W. The significance of fatigue crack closure under cyclic tension. ASTM STP 1971; 486:230-242.

[13] Vasudevan AK, Sadananda K, Louat N. (1993) Two critical stress intensities for threshold crack propagation. Scripta Metallurgica et Materialia, 28, 65–70.

[14] Kujawski D. A new $(\Delta K^+ K_{max})^{0.5}$ driving force parameter for crack growth in aluminum alloys. Int J Fatigue 2001;23:733–740.

[15] Christopher CJ, James MN, Patterson EA, Tee KF. Towards a new model of crack tip stress fields. Int J Fract 2007;148:361–371.

[16] Paul SK, Tarafder S. Cyclic plastic deformation response at fatigue crack tips. Int Journal of Pressure Vessels and Piping 2013;101:81-90.

[17] Ritchie RO. Why Ductile Fracture Mechanics? J Eng Mat Tech 1983;105:1-7.

[18] Rice JR. Mechanisms of Crack Tip Deformation and Extension by Fatigue. Fatigue Crack Propagation, ASTM STP 415 1967;247-309.

[19] Cadario A, Alfredsson B. Fatigue growth of short cracks in Ti-17: Experiments and simulations. Eng Fract Mech 2007;74:2293–2310.

[20] Tvergaard V. On fatigue crack growth in ductile materials by crack–tip blunting. Journal of the Mechanics and Physics of Solids 2004;52:2149 – 2166.

[21] Bodner SR, Davidson DL, Lankford J. A description of fatigue crack growth in terms of plastic work. Eng Fract Mech 1983;17(2):189–191.

[22] Ravi Chandran KS. Mechanics of fatigue crack growth under large-scale plasticity: A direct physical approach for single-valued correlation of fatigue crack growth data. Int J Fatigue 2018;117:299–313.

[23] Ould Chikh B, Imad A, Benguediab M. (2008). Influence of the cyclic plastic zone size on the propagation of the fatigue crack in case of 12NC6 steel. Comput Mat Science, 43, 1010–1017.

[24] Dezecot S, Rambaudon M, Koster A, Szmytka F, Maurel V, Buffiere J-Y. Fatigue crack growth under large scale yielding condition in a cast automotive aluminum alloy. Mat Science & Eng A 2019;743:87–97.

[25] Leopold G, Muniera R. Crack propagation in Large Scale Yielding (LSY) conditions. Proc Eng 2015;133:681-687.

[26] Schweizer C, Schlesinger M, Oesterlin H, Friedmann V, Bednarz P, Meilgen C, Szwedowicz J. Methodology for fatigue crack growth testing under large scale yielding conditions on corner-crack specimens. Eng Fract Mech 2014;126:126–140.

[27] Dowling NE. Mechanical Behaviour of materials. New Jersey, Prentice Hall 1999.

[28] Antunes FV, Sousa T, Branco R, Correia L. Effect of crack closure on non-linear crack tip parameters. Int J Fatigue 2015;71:53–63.

[29] Frederick CO, Armstrong PJ. A mathematical representation of the multiaxial Bauschinger effect. Mater High Temp 2007;24:1–26.

[30] Voce E. The Relationship Between Stress and Strain for Homogeneous Deformation. J Inst Met 1948;74:537–562.

[31] Swift HW. Plastic instability under plane stress. Journal of the Mechanics and Physics of Solids 1952;1:1–18.

[32] Antunes FV, Serrano S, Branco R, Prates P. Fatigue crack growth in the 2050-T8 aluminium alloy, Int J Fatigue 2018;115:79–88.

[33] Antunes FV, Ferreira MSC, Branco R, Prates P, Gardin C, Sarrazin-Baudoux C. Fatigue crack growth versus plastic CTOD in the 304L stainless steel. Eng Fract Mech 2019;214:487–503.

[34] Antunes FV, Branco R, Prates PA, Borrego L. Fatigue crack growth modelling based on CTOD for the 7050-T6 alloy. Fat Fract Eng Mater Struct 2017;40(8):1309–1320.

[35] Antunes FV, Rodrigues SM, Branco R, Camas D. A numerical analysis of CTOD in constant amplitude fatigue crack growth. Theor Appl Fract Mech 2016;85:45–55.

[36] Antunes FV, Santos L, Capela C, Ferreira JM, Costa JD, Jesus J, Prates P. Fatigue Crack Growth in Maraging Steel obtained by Selective Laser Melting. Applied Science 2019;9:4412.

[37] Borges MF, Neto DM, Antunes FV. Numerical simulation of fatigue crack growth based on accumulated plastic strain. Theor Appl Fract Mech 2020;108:102676.

[38] Marques B, Neto DM, Antunes FV, Vasco-Olmo JM, Díaz FA. Numerical tool for the analysis of CTOD curves obtained by DIC or FEM. Fat Fract Eng Mater Struct 2020;43:2984–2997.

[39] Escalero M, Muniz-Calvente M, Zabal H, Urrestia I. Suitability of constraint and closure models for predicting crack growth in generic configurations. Eng Fract Mech 2020;225:106808.

[40] Tammas-Williams S, Withers PJ, Todd I, Prangnell B. The Effectiveness of Hot Isostatic Pressing for Closing Porosity in Titanium Parts Manufactured by Selective Electron Beam Melting. Metall Mat Trans A 2016;47A:1-8.

[41] Vasco-Olmo JM, Díaz FA, Antunes FV, James MN. Characterisation of fatigue crack growth using digital image correlation measurements of plastic CTOD. Theor Appl Fract Mech 2019;101:332–341.